

# On the Construction, Comparison, and Local Characteristic Decomposition for High-Order Central WENO Schemes

Jianxian Qiu<sup>\*,1</sup> and Chi-Wang Shu<sup>†,2</sup>

<sup>\*</sup>Department of Mathematics, University of Science and Technology of China, Hefei, Anhui 230026, People's Republic of China; and <sup>†</sup>Division of Applied Mathematics, Brown University, Providence, Rhode Island 02912  
E-mail: jxqiu@ustc.edu.cn, shu@cfm.brown.edu

Received September 12, 2001; revised May 23, 2002

---

In this paper, we review and construct fifth- and ninth-order central weighted essentially nonoscillatory (WENO) schemes based on a finite volume formulation, staggered mesh, and continuous extension of Runge–Kutta methods for solving nonlinear hyperbolic conservation law systems. Negative linear weights appear in such a formulation and they are treated using the technique recently introduced by Shi *et al.* (*J. Comput. Phys.* **175**, 108 (2002)). We then perform numerical computations and comparisons with the finite difference WENO schemes of Jiang and Shu (*J. Comput. Phys.* **150**, 97 (1999)) and Balsara and Shu (*J. Comput. Phys.* **160**, 405 (2000)). The emphasis is on the performance with or without a local characteristic decomposition. While this decomposition increases the computational cost, we demonstrate by our numerical experiments that it is still necessary to use it to control spurious oscillations when the order of accuracy is high, both for the central staggered grid and for the upwind nonstaggered grid WENO schemes. We use the shock entropy wave interaction problem to demonstrate the advantage of using higher order WENO schemes when both shocks and complex solution features coexist. © 2002 Elsevier Science (USA)

*Key Words:* WENO scheme; central scheme; high-order accuracy; local characteristic decomposition.

---

## 1. INTRODUCTION

In this paper, we review and construct fifth- and ninth-order central weighted essentially nonoscillatory (WENO) schemes based on a finite volume formulation, staggered mesh, and continuous extension of Runge–Kutta methods for solving nonlinear hyperbolic

<sup>1</sup> The research of this author was supported in part by NSFC Grants 59979004 and 10028103.

<sup>2</sup> The research of this author was supported in part by NSFC Grant 10028103 while he was in residence at the Department of Mathematics, University of Science and Technology of China, Hefei, Anhui 230026, P.R. China. Additional support was provided by ARO Grant DAAD19-00-1-0405 and NSF Grant DMS-9804985.

conservation law systems

$$\begin{aligned}u_t + \nabla \cdot f(u) &= 0 \\ u(x, 0) &= u_0(x).\end{aligned}\tag{1.1}$$

Only the one-dimensional case is considered in this paper, although with some nontrivial efforts the algorithm can be extended to multiple dimensions along the lines of [1, 2, 8, 9, 13, 16, 18]. Negative linear weights appear in such a formulation and they are treated using the technique recently introduced by Shi *et al.* [25]. We then perform numerical computations and comparisons with the finite difference WENO schemes of Jiang and Shu [7] and Balsara and Shu [3]. The emphasis is on the performance with or without a local characteristic decomposition. While this decomposition increases the computational cost, we demonstrate by our numerical experiments that it is still necessary to use it to control spurious oscillations when the order of accuracy is high, both for the central staggered grid or upwind nonstaggered grid WENO schemes. We use the shock entropy wave interaction problem to demonstrate the advantage of using higher order WENO schemes when both shocks and complex solution features coexist.

The central schemes are extensions of the Lax–Friedrichs (LxF) scheme. The LxF scheme is very simple and robust, but it is only first-order accurate and excessively diffusive. In 1990, Nessyahu and Tadmor [23] developed a class of nonoscillatory second-order central difference approximations to hyperbolic conservation laws in one spatial dimension (the NT schemes). These approximations can be viewed as a natural extension of the LxF scheme and are total variation diminishing in the scalar one-dimensional case. For the system case, these second-order central schemes require no Riemann solvers, no local characteristic decompositions, and no flux splitting. Therefore, all that one has to do in order to solve (1.1) is to supply the flux function  $f(u)$ . Thus the NT central schemes are simpler than most upwind schemes (they are comparable in simplicity and cost with upwind schemes using a Lax–Friedrichs building block and componentwise limiting or ENO/WENO reconstruction), especially for cases where the complete set of eigenvectors of the Jacobian  $f'(u)$  is difficult to obtain or it does not exist (such as for the weakly hyperbolic systems). For these reasons the NT schemes and their extensions have become quite popular in applications. After the pioneer work of Nessyahu and Tadmor in [23], many different central schemes have been developed [4, 8–18, 21, 24]. A major difference among different central schemes is in the reconstruction step, where one computes a piecewise polynomial interpolation from the cell averages. The second-order NT scheme [23] and its extension to two dimensions [1, 2, 8, 9] are based on a MUSCL-like piecewise linear interpolant and nonlinear limiters to prevent spurious oscillations; the third-order scheme by Liu and Tadmor [21] is based on a quadratic interpolant developed by Liu and Osher [20]; the third-order and fourth-order schemes by Bianco *et al.* [4] are based on a modified ENO reconstruction of point values from cell averages, and on numerical fluxes on cell boundaries. The reconstruction of the  $x$ -derivatives of  $f(u)$  is performed from interpolation of grid values of  $f(u)$ , and the evaluation of the fluxes is obtained through a Runge–Kutta method with the aid of the so-called natural continuous extension (NCE) [30]. The use of this NCE Runge–Kutta technique lowers the computational cost. In the spirit of Godunov-type schemes, Levy *et al.* [16, 18] presented a third-order central scheme for approximating solutions of systems of conservation laws in one and two space dimensions. The method is based on reconstructing a piecewise-polynomial interpolant from cell averages, which is then advanced in time. In the reconstruction step, a third-order, compact, central weighted essentially nonoscillatory

(CWENO) reconstruction is introduced, which is written as a convex combination of interpolants based on different stencils. In the one-dimensional case, the third-order reconstruction is based on an extremely compact three-point stencil. Analogous compactness is retained in more space dimensions. Higher order CWENO schemes are developed in [15]. In contrast to the NT scheme that is based on cell averages, schemes by Liu and Osher [19] are based on point values and the general ENO philosophy, removing the need for staggered grids thus getting rid of the associated difficulties at the boundary.

The first WENO scheme is constructed in [22] for a third-order finite volume version in one space dimension. In [7], third- and fifth-order finite difference WENO schemes in multiple space dimensions are constructed, with a general framework for the design of the smoothness indicators and nonlinear weights. WENO schemes are designed based on the successful ENO schemes in [5, 28, 29]. Both ENO and WENO schemes use the idea of adaptive stencils in the reconstruction procedure based on the local smoothness of the numerical solution to automatically achieve high-order accuracy and a nonoscillatory property near discontinuities. ENO uses just one (optimal in some sense) out of many candidate stencils when doing the reconstruction; while WENO uses a convex combination of all the candidate stencils, each being assigned a nonlinear weight which depends on the local smoothness of the numerical solution based on that stencil. WENO improves upon ENO in robustness, better smoothness of fluxes, better steady-state convergence, better provable convergence properties, and more efficiency. Third- and fourth-order triangle-based finite volume WENO schemes can be found in [6]. For a detailed review of ENO and WENO schemes, we refer to [27].

Levy *et al.* [15] designed central WENO schemes up to fourth order. A key idea in WENO schemes is a linear combination of lower order fluxes or reconstruction to obtain a higher order approximation. The combination coefficients, also called linear weights, are determined by local geometry of the mesh and order of accuracy and may become negative. WENO procedures cannot be applied directly to obtain a stable scheme if negative linear weights are present. A previous strategy for handling this difficulty was by either regrouping stencils or reducing the order of accuracy to get rid of the negative linear weights. In [25], Shi *et al.* presented a simple and effective technique for handling negative linear weights without a need to get rid of them. This technique is used in our work for designing fifth- and ninth-order central WENO schemes.

The organization of this paper is as follows. In Section 2 we review and construct fifth- and ninth-order CWENO schemes based on a finite volume formulation, staggered mesh, and continuous extension of Runge–Kutta methods for solving one-dimensional nonlinear hyperbolic conservation laws. In Section 3 we perform numerical computations and comparisons with the finite difference WENO schemes of Jiang and Shu [7] and Balsara and Shu [3]. The emphasis is on the performance with or without a local characteristic decomposition. We also use the shock entropy wave interaction problem to demonstrate the advantage of using higher order WENO schemes when both shocks and complex solution features coexist. Concluding remarks are given in Section 4.

## 2. FIFTH- AND NINTH-ORDER CENTRAL WENO SCHEMES

In this section we consider one-dimensional conservation laws

$$u_t + f(u)_x = 0. \quad (2.1)$$

For simplicity, we assume that the grid points  $\{x_i\}$  are uniform with  $x_{i+1} - x_i = h$ , and  $x_{i+\frac{1}{2}} = \frac{1}{2}(x_i + x_{i+1})$ . We also denote the cells  $I_i = [x_{i-\frac{1}{2}}, x_{i+\frac{1}{2}}]$ ,  $I_{i+\frac{1}{2}} = [x_i, x_{i+1}]$ . Let  $k$  be the time step,  $t^{n+1} = t^n + k$ ;  $u_i^n = u(x_i, t^n)$  denotes the point values, and  $\bar{u}_i^n = \frac{1}{h} \int_{I_i} u(x, t^n) dx$ ,  $\bar{u}_{i+\frac{1}{2}}^n = \frac{1}{h} \int_{I_{i+\frac{1}{2}}} u(x, t^n) dx$  represent the cell averages at time  $t^n$  on the cells  $I_i$  and  $I_{i+\frac{1}{2}}$ , respectively.<sup>2</sup> The CWENO scheme approximates the cell averages at time  $t^{n+1}$  based on their values at time  $t^n$  with staggered space grids. Following [15, 23], we integrate (2.1) over the region  $I_{i+\frac{1}{2}} \times [t^n, t^{n+1}]$  to get an equivalent formulation of the conservation laws (2.1):

$$\bar{u}_{i+\frac{1}{2}}^{n+1} = \bar{u}_{i+\frac{1}{2}}^n - \frac{1}{h} \left[ \int_{t^n}^{t^{n+1}} f(u(x_{i+1}, t)) dt - \int_{t^n}^{t^{n+1}} f(u(x_i, t)) dt \right]. \quad (2.2)$$

This finite volume formulation expresses the precise relation between the sliding averages and the underlying point values. We will use this formulation (2.2) as the starting point for the construction of high-order CWENO schemes. We want to find approximations of the cell averages  $\bar{u}_{i+\frac{1}{2}}^n$  and the two integrals in (2.2). Thus the algorithm consists of two major steps to evolve from  $\{\bar{u}_i^n\}$  to  $\{\bar{u}_{i+\frac{1}{2}}^{n+1}\}$ :

Step 1: The approximation of  $\bar{u}_{i+\frac{1}{2}}^n$  from  $\{\bar{u}_i^n\}$  by a WENO reconstruction. Notice that

$$\bar{u}_{i+\frac{1}{2}}^n = \frac{1}{h} \int_{x_i}^{x_{i+1}} u(x, t^n) dx = \frac{1}{h} \left[ \int_{x_i}^{x_{i+\frac{1}{2}}} u(x, t^n) dx + \int_{x_{i+\frac{1}{2}}}^{x_{i+1}} u(x, t^n) dx \right];$$

hence we only need to reconstruct  $\frac{1}{h} \int_{x_{i-\frac{1}{2}}}^{x_i} u(x, t^n) dx$  for all  $i$  because

$$\frac{1}{h} \int_{x_i}^{x_{i+\frac{1}{2}}} u(x, t^n) dx = \bar{u}_i^n - \frac{1}{h} \int_{x_{i-\frac{1}{2}}}^{x_i} u(x, t^n) dx \quad (2.3)$$

by conservation. This step is achieved in the following steps:

1. We identify  $r$  small stencils  $S_j$ ,  $j = 0, \dots, r-1$ , such that  $I_i$  belongs to each of them. Here we set  $S_j = \cup_{l=0}^{r-1} I_{i+j-l}$ . We denote by  $\mathcal{T} = \cup_{j=0}^{r-1} S_j$  the larger stencil which contains all the cells from the  $r$  smaller stencils.

2. We have a  $(r-1)$ th degree polynomial reconstruction denoted by  $p_j(x)$ , associated with each of the stencils  $S_j$ ,  $j = 0, \dots, r-1$ , such that the cell average of  $p_j(x)$  in each of the cells in the stencil  $S_j$  agrees with the given cell average of  $u$ ; i.e.,  $\frac{1}{h} \int_{I_{i+j-l}} p_j(x) dx = \bar{u}_{i+j-l}$ ,  $l = 0, \dots, r-1$ . We also have a higher order  $(2r-2)$ th degree polynomial reconstruction denoted by  $Q(x)$ , associated with the larger stencil  $\mathcal{T}$ , such that  $\frac{1}{h} \int_{I_{i+l}} Q(x) dx = \bar{u}_{i+l}$ ,  $l = -r+1, \dots, r-1$ . The detail of the construction of  $p_j(x)$  and  $Q(x)$  can be found in [27].

3. We find the combination coefficients, also called linear weights, denoted by  $\gamma_0, \dots, \gamma_{r-1}$ , such that

$$\int_a^b Q(x) dx = \sum_{j=0}^{r-1} \gamma_j \int_a^b p_j(x) dx \quad (2.4)$$

for all possible given cell averages of  $u$  in the stencils. These linear weights depend on the mesh geometry and integral interval  $[a, b]$ , but not on the given solution  $u$  in the stencils.

Here in order to compute the approximation of  $\frac{1}{h} \int_{x_i}^{x_{i+\frac{1}{2}}} u(x, t^n) dx$  or  $\frac{1}{h} \int_{x_{i-\frac{1}{2}}}^{x_i} u(x, t^n) dx$ , we can just set  $[a, b] = [x_i, x_{i+\frac{1}{2}}]$  or  $[a, b] = [x_{i-\frac{1}{2}}, x_i]$ . For example, when  $r \equiv 3$  and  $r = 5$ , we have

$$\int_{x_{i-\frac{1}{2}}}^{x_i} p_j(x) dx = \sum_{l=0}^{r-1} a_{jl} \bar{u}_{i+j+l-r+1}, \quad j=0, \dots, r-1 \quad (2.5)$$

with

$$A = (a_{jl})_{3 \times 3} = \begin{pmatrix} -\frac{1}{16} & \frac{1}{4} & \frac{5}{16} \\ \frac{1}{16} & \frac{1}{2} & -\frac{1}{16} \\ \frac{11}{16} & -\frac{1}{4} & \frac{1}{16} \end{pmatrix}$$

$$\gamma_0 = \frac{3}{16}, \quad \gamma_1 = \frac{5}{8}, \quad \gamma_2 = \frac{3}{16}$$

for  $r = 3$  (see [15]), and

$$A = (a_{jl})_{5 \times 5} = \begin{pmatrix} \frac{7}{256} & -\frac{19}{128} & \frac{11}{32} & -\frac{61}{128} & \frac{193}{256} \\ -\frac{3}{256} & \frac{9}{128} & -\frac{13}{64} & \frac{79}{128} & \frac{7}{256} \\ \frac{3}{256} & -\frac{11}{128} & \frac{1}{2} & \frac{11}{128} & -\frac{3}{256} \\ -\frac{7}{256} & \frac{49}{128} & \frac{13}{64} & -\frac{9}{128} & \frac{3}{256} \\ \frac{63}{256} & \frac{61}{128} & -\frac{11}{32} & \frac{19}{128} & -\frac{7}{256} \end{pmatrix}$$

$$\gamma_0 = \frac{5}{256}, \quad \gamma_1 = \frac{15}{64}, \quad \gamma_2 = \frac{63}{128}, \quad \gamma_3 = \frac{15}{64}, \quad \gamma_4 = \frac{5}{256}$$

for  $r = 5$ .

Similarly,

$$\int_{x_i}^{x_{i+\frac{1}{2}}} p_j(x) dx = \sum_{l=0}^{r-1} b_{jl} \bar{u}_{i+j+l-r+1}, \quad j=0, \dots, r-1 \quad (2.6)$$

with

$$B = (b_{jl})_{3 \times 3} = \begin{pmatrix} \frac{1}{16} & -\frac{1}{4} & \frac{11}{16} \\ -\frac{1}{16} & \frac{1}{2} & \frac{1}{16} \\ \frac{5}{16} & \frac{1}{4} & -\frac{1}{16} \end{pmatrix}$$

$$\gamma_0 = \frac{3}{16}, \quad \gamma_1 = \frac{5}{8}, \quad \gamma_2 = \frac{3}{16}$$

for  $r = 3$ , and

$$B = (b_{jl})_{5 \times 5} = \begin{pmatrix} -\frac{7}{256} & \frac{19}{128} & -\frac{11}{32} & \frac{61}{128} & \frac{63}{256} \\ \frac{3}{256} & -\frac{9}{128} & \frac{13}{64} & \frac{49}{128} & -\frac{7}{256} \\ -\frac{3}{256} & \frac{11}{128} & \frac{1}{2} & -\frac{11}{128} & \frac{3}{256} \\ \frac{7}{256} & \frac{79}{128} & -\frac{13}{64} & \frac{9}{128} & -\frac{3}{256} \\ \frac{193}{256} & -\frac{61}{128} & \frac{11}{32} & -\frac{19}{128} & \frac{7}{256} \end{pmatrix}$$

$$\gamma_0 = \frac{5}{256}, \quad \gamma_1 = \frac{15}{64}, \quad \gamma_2 = \frac{63}{128}, \quad \gamma_3 = \frac{15}{64}, \quad \gamma_4 = \frac{5}{256}$$

for  $r = 5$ .

Notice that the linear weights  $\gamma_j$  are the same for the subintervals  $[x_i, x_{i+\frac{1}{2}}]$  and  $[x_{i-\frac{1}{2}}, x_i]$ . Hence if we use WENO reconstruction to compute one of them and then use the conservation (2.3) to get the other, the result does not depend on which one we choose to compute by WENO.

4. We compute the smoothness indicator, denoted by  $\beta_j$ , for each stencil  $S_j$ , which measures how smooth the function  $p_j(x)$  is in the target cell  $I_i$ . The smaller this smoothness indicator  $\beta_j$ , the smoother the function  $p_j(x)$  is in the target cell. In all of the current WENO schemes we use the following smoothness indicator:

$$\beta_j = \sum_{l=1}^{r-1} \int_{I_i} h^{2l-1} \left( \frac{d^l}{dx^l} p_j(x) \right)^2 dx. \quad (2.7)$$

Notice that in the actual numerical implementation the smoothness indicators  $\beta_j$  are written out explicitly as quadratic forms of the cell averages of  $u$  in the stencil; see [3, 7, 27] for details.

5. We compute the nonlinear weights based on the smoothness indicators

$$\omega_j = \frac{\bar{\omega}_j}{\sum_{l=0}^{r-1} \bar{\omega}_l}, \quad \bar{\omega}_j = \frac{\gamma_j}{(\varepsilon + \beta_j)^2}, \quad (2.8)$$

where  $\gamma_j$  are the linear weights determined in step 3 above, and  $\varepsilon$  is a small number to avoid the denominator to become 0. We use  $\varepsilon = 10^{-8}$  in all the computations in this paper. The final WENO approximation is then given by

$$\frac{1}{h} \int_{x_i}^{x_{i+\frac{1}{2}}} u(x, t^n) dx \approx \sum_{j=0}^{r-1} \omega_j \int_{x_i}^{x_{i+\frac{1}{2}}} p_j(x) dx$$

or

$$\frac{1}{h} \int_{x_{i-\frac{1}{2}}}^{x_i} u(x, t^n) dx \approx \sum_{j=0}^{r-1} \omega_j \int_{x_{i-\frac{1}{2}}}^{x_i} p_j(x) dx.$$

Again, only one of them must be computed because of the conservation property (2.3). The result does not depend on which one we choose to compute by WENO.

This step produces a reconstruction of  $\bar{u}_{i+\frac{1}{2}}^n$ , which is  $(2r - 1)$ th order accurate. We use  $r = 3$  and  $r = 5$  in this paper to obtain fifth- and ninth-order WENO reconstructions in this step, respectively. Notice that the WENO stencil in this reconstruction is central. No upwind mechanism is involved.

Step 2: The approximation of  $\int_{t^n}^{t^{n+1}} f(u(x_i, t)) dt$ . If the time step  $k$  is subject to a restrictive CFL condition  $k \leq \frac{h}{2} \max |f'(u)|$ , we can assume that  $u(x_i, t)$  is smooth, since the discontinuities starting at  $t^n$  from the staggered grid points  $x_{i-\frac{1}{2}}$  and  $x_{i+\frac{1}{2}}$  have not reached the cell boundary  $x_i$  yet. Hence no Riemann solvers are needed and the time integrals can be evaluated with a quadrature formula to high-order accuracy. Notice that this is equivalent

to a Lax–Friedrichs scheme and the same effect can also be achieved without a staggered mesh by just using a Lax–Friedrichs building block, such as those WENO finite difference schemes in [3, 7], where the Lax–Friedrichs building blocks are used and no Riemann solvers are needed. In this paper we use a three-point Gauss quadrature formula. That is,

$$\int_{t^n}^{t^{n+1}} f(u(x_i, t)) dt \approx k \sum_{l=1}^3 \alpha_l f(u(x_i, t^n + k\tau_l)),$$

where  $\alpha_1 = \alpha_3 = \frac{5}{18}$ ,  $\alpha_2 = \frac{4}{9}$ , and  $\tau_1 = \frac{1}{2} - \frac{\sqrt{15}}{10}$ ,  $\tau_2 = \frac{1}{2}$ ,  $\tau_3 = \frac{1}{2} + \frac{\sqrt{15}}{10}$  are the weights and knots of the Gauss quadrature formula.

Now we want to find the approximation of the point values  $u(x_i, t^n + k\tau_l)$  from the cell averages  $\{\bar{u}_i^n\}$ . We consider the conservation laws at the grid points  $x = x_i$ . At each of these points, the PDE (2.1) reduces to an autonomous ODE in the time variable  $t$ .

$$\begin{aligned} \frac{du(x_i, t)}{dt} &= -(f(u))_x|_{x_i} \\ u(x_i, t^n) &\approx u_i^n. \end{aligned} \tag{2.9}$$

Here  $u_i^n$  will be computed by reconstruction from the cell averages  $\{\bar{u}_i^n\}$ , and the ODE (2.9) will be solved by the classical fourth-order Runge–Kutta method to obtain the approximation of  $u(x_i, t^n + k\tau_l)$ .

This step thus consists of the following steps:

1. WENO reconstruction of  $u_i^n \approx u(x_i, t^n)$  is described. The process of the WENO reconstruction of  $u_i^n$  basically follows the steps 1 to 5 in Step 1 above, with a change in step 3 to the following:

We find the linear weights, denoted by  $\gamma_0, \dots, \gamma_{r-1}$ , such that

$$Q(x_i) = \sum_{j=0}^{r-1} \gamma_j p_j(x_i) \tag{2.10}$$

for all possible given data in the stencils. These linear weights depend on the mesh geometry and the point  $x_i$ , but not on the given solution data in the stencils. Notice that, as before, this step produces a reconstruction of  $u_i^n$ , which is  $(2r - 1)$ th-order accurate. We use  $r = 3$  and  $r = 5$  again to obtain fifth- and ninth-order WENO reconstructions in this step, respectively. The WENO stencil in this reconstruction is again central. No upwind mechanism is involved. The polynomials  $p_j(x)$  involved here are the same as those in the first step above to reconstruct  $\bar{u}_{i+\frac{1}{2}}^n$ ; hence the smoothness indicators (2.7) do not need to be recomputed.

For example, when  $r = 3$  and  $r = 5$ , we have

$$p_j(x_i) = \sum_{l=0}^{r-1} c_{jl} \bar{u}_{i+j+l-r+1}, \quad j = 0, \dots, r-1 \tag{2.11}$$

with

$$C = (c_{jl})_{3 \times 3} = \begin{pmatrix} -\frac{1}{24} & \frac{1}{12} & \frac{23}{24} \\ \frac{1}{24} & \frac{13}{12} & -\frac{1}{24} \\ \frac{23}{24} & \frac{1}{12} & -\frac{1}{24} \end{pmatrix}$$

$$\gamma_0 = -\frac{9}{80}, \quad \gamma_1 = \frac{49}{40}, \quad \gamma_2 = -\frac{9}{80}$$

for  $r = 3$ , and

$$C = (c_{jl})_{5 \times 5} = \begin{pmatrix} -\frac{71}{1920} & \frac{91}{480} & -\frac{373}{960} & \frac{57}{160} & \frac{563}{640} \\ \frac{3}{640} & -\frac{3}{160} & -\frac{13}{960} & \frac{511}{480} & -\frac{71}{1920} \\ \frac{3}{640} & -\frac{29}{480} & \frac{1067}{960} & -\frac{29}{480} & \frac{3}{640} \\ -\frac{71}{1920} & \frac{511}{480} & -\frac{13}{960} & -\frac{3}{160} & \frac{3}{640} \\ \frac{563}{640} & \frac{57}{160} & -\frac{373}{960} & \frac{91}{480} & -\frac{71}{1920} \end{pmatrix}$$

$$\gamma_0 = -\frac{525}{163584}, \quad \gamma_1 = -\frac{63425}{286272}, \quad \gamma_2 = \frac{11689}{8064}, \quad \gamma_3 = -\frac{63425}{286272}, \quad \gamma_4 = -\frac{525}{163584}$$

for  $r = 5$ .

We remark that it is easy to verify that, when  $r$  is an even number ( $r = 2, 4, \dots$ ), there are no linear weights that satisfy condition (2.10). Hence there are no third-, seventh-, eleventh-, etc., order central WENO reconstructions for the point values  $u_i^n$  with these choices of stencils.

From (2.11) we notice that two of the linear weights are negative. When linear weights become negative, the usual WENO approximation is unstable. Here we adopt the splitting technique of treating negative weights in WENO schemes developed by Shi *et al.* [25]: We first split the linear weights into two groups

$$\tilde{\gamma}_i^+ = \frac{1}{2}(\gamma_i + 3|\gamma_i|), \quad \tilde{\gamma}_i^- = \tilde{\gamma}_i^+ - \gamma_i, \quad i = 0, \dots, r - 1$$

and scale them by

$$\sigma^\pm = \sum_{j=0}^{r-1} \tilde{\gamma}_j^\pm; \quad \gamma_i^\pm = \tilde{\gamma}_i^\pm / \sigma^\pm, \quad i = 1, \dots, r - 1.$$

For example, when  $r = 3$ , we obtain

$$\gamma_0^+ = \frac{9}{80}, \quad \gamma_1^+ = \frac{49}{20}, \quad \gamma_2^+ = \frac{9}{80}; \quad \gamma_0^- = \frac{9}{40}, \quad \gamma_1^- = \frac{49}{40}, \quad \gamma_2^- = \frac{9}{40},$$

and

$$\sigma^+ = \frac{107}{40}, \quad \sigma^- = \frac{67}{40};$$

$$\gamma_0^+ = \frac{9}{214}, \quad \gamma_1^+ = \frac{98}{107}, \quad \gamma_2^+ = \frac{9}{214}; \quad \gamma_0^- = \frac{9}{67}, \quad \gamma_1^- = \frac{49}{67}, \quad \gamma_2^- = \frac{9}{67}.$$

The WENO reconstruction is now performed on each group separately, by computing the nonlinear weights (2.8) separately for  $\omega_j^\pm$  with the same smoothness indicators  $\beta_j$  as those in (2.7). The final WENO reconstruction is then taken as  $\sigma^+$  times the reconstruction using the group of positive weights minus  $\sigma^-$  times the reconstruction using the group of negative weights. The key idea of this decomposition is to ensure that every stencil has a significant

representation in both the positive and the negative weight groups. Within each group, the WENO idea of redistributing the weights subject to a fixed sum according to the smoothness of the approximation is still followed as before. For more details, we refer to [25].

2. The Runge–Kutta method with the aid of natural continuous extension for (2.9) is described. If the classical fourth-order Runge–Kutta method is used to compute each of the  $u(x_i, t^n + k\tau_l)$  to fourth-order accuracy, we would need to reconstruct  $f_x$  four times for each  $u(x_i, t^n + k\tau_l)$ . This would become extremely costly. Bianco *et al.* [4] initiated a strategy to achieve a significant saving in computational cost by using the NCE of a Runge–Kutta scheme developed by Zennaro [30]. This is the strategy we will also use in this paper.

For simplicity we shall only describe the fourth-order NCE Runge–Kutta method which will be used in this paper. Further details about NCE can be found in [4, 30]. Consider the Cauchy problem,

$$\begin{aligned} y'(t) &= F(t, y(t)) \\ y(t_0) &= y_0, \end{aligned} \tag{2.12}$$

the solution at the  $(n + 1)$ th time step obtained with the traditional fourth-order Runge–Kutta scheme can be written as

$$y^{n+1} = y^n + k \sum_{j=1}^4 b_j g^{(j)},$$

where  $b_1 = b_4 = \frac{1}{6}$ ,  $b_2 = b_3 = \frac{1}{3}$ , and the  $g^{(j)}$  are the approximate Runge–Kutta fluxes

$$\begin{aligned} g^{(1)} &= F(t^n, y^n) \\ g^{(2)} &= F\left(t^n + c_2 k, y^n + \frac{k}{2} g^{(1)}\right) \\ g^{(3)} &= F\left(t^n + c_3 k, y^n + \frac{k}{2} g^{(2)}\right) \\ g^{(4)} &= F\left(t^n + c_4 k, y^n + k g^{(3)}\right) \\ c_2 = c_3 &= \frac{1}{2}, c_4 = 1. \end{aligned}$$

For this Runge–Kutta scheme there exist four third-order polynomials

$$\begin{aligned} b_1(\theta) &= 2(1 - 4b_1)\theta^3 + 3(3b_1 - 1)\theta^2 + \theta, \\ b_j(\theta) &= 4(3c_j - 2)b_j\theta^3 + 3(3 - 4c_j)b_j\theta^2, \quad j = 2, 3, 4 \end{aligned}$$

such that the natural continuous extension  $z$  of degree 3 satisfies

$$\begin{aligned} z(t^n + \theta k) &:= y^n + k \sum_{j=1}^4 b_j(\theta) g^{(j)}, \quad 0 \leq \theta \leq 1; \\ z(t^n) &= y^n \quad \text{and} \quad z(t^{n+1}) = y^{n+1}; \\ \max_{t^n \leq t \leq t^{n+k}} |y^{(l)}(t) - z^{(l)}(t)| &= O(k^{4-l}), \quad 0 \leq l \leq 4, \end{aligned}$$

where  $y(t)$  is the exact solution of (2.12) with  $y(t^n) = y^n$ .

Thus at each time step, we apply the Runge–Kutta scheme only once and obtain all the intermediate values  $u(x_i, t^n + k\tau_i)$  to fourth-order accuracy through the evaluation of the NCE.

3. The WENO approximation of  $f(u)_x|_{x=x_i}$  from  $\{u_i = u(x_i, t)\}$  is described. We denote  $f_i = f(u_i)$ . This step consists of the following steps:

(a) We identify several point sets  $S_j$ ,  $j = 0, \dots, r - 1$ , such that  $x_i$  belongs to each of them. Here we set  $S_j = \cup_{l=0}^{r-1} x_{i+j-l}$ . We denote by  $\mathcal{T} = \cup_{j=0}^{r-1} S_j$  the larger set which contains all the points from the  $r$  smaller sets.

(b) We have a  $(r - 1)$ th degree interpolating polynomial function denoted by  $p_j(x)$ , associated with each of the sets  $S_j$ ,  $j = 0, \dots, r - 1$ , such that  $p_j(x_{i+j-l}) = f_{i+j-l}$ ,  $l = 0, \dots, r - 1$ . We also have a higher  $(2r - 2)$ th degree interpolating polynomial function denoted by  $Q(x)$ , associated with the larger set  $\mathcal{T}$ , such that  $Q(x_{i+l}) = f_{i+l}$ ,  $l = -r + 1, \dots, r - 1$ .

(c) We find the linear weights, denoted by  $\gamma_0, \dots, \gamma_{r-1}$ , such that

$$Q'(x_i) = \sum_{j=0}^{r-1} \gamma_j p'_j(x_i) \quad (2.13)$$

for all possible given data in the set. These linear weights depend on the mesh geometry and the point  $x_i$ , but not on the given solution data in the set.

In this paper we set  $r = 3$  and  $r = 5$  for the fourth- and eighth-order accurate approximation to the derivative  $f(u)_x|_{x=x_i}$ , yielding fifth- and ninth-order schemes. We again notice that this approximation to  $f(u)_x|_{x=x_i}$  is purely central. No upwind mechanism is present. If we would like to introduce some upwinding mechanism (artificial viscosity at the level of truncation error), we could perform a Lax–Friedrich flux splitting

$$f^\pm(u) = \frac{1}{2}(f(u) \pm \alpha u), \quad \alpha = \max_u |f'(u)|,$$

where the maximum is taken over  $u_i^n$  for all  $i$ . We could then use one more grid point, added either to the left for  $f^+(u)$  or to the right for  $f^-(u)$ , in the approximation to the derivatives  $f^\pm(u)_x|_{x=x_i}$ .

For example, when  $r = 3$  and  $r = 5$ , we have

$$p'_j(x_i) = \sum_{l=0}^{r-1} d_{jl} f_{i+j+l-r+1}, \quad j = 0, \dots, r - 1 \quad (2.14)$$

with

$$D = (d_{jl})_{3 \times 3} = \begin{pmatrix} \frac{1}{2} & -2 & \frac{3}{2} \\ -\frac{1}{2} & 0 & \frac{1}{2} \\ -\frac{3}{2} & 2 & -\frac{1}{2} \end{pmatrix}$$

$$\gamma_0 = \frac{1}{6}, \quad \gamma_1 = \frac{2}{3}, \quad \gamma_2 = \frac{1}{6}$$

for  $r = 3$  (see [15]), and

$$D = (d_{jl})_{5 \times 5} = \begin{pmatrix} \frac{1}{4} & -\frac{4}{3} & 3 & -4 & \frac{25}{12} \\ -\frac{1}{12} & \frac{1}{2} & -\frac{3}{2} & \frac{5}{6} & \frac{1}{4} \\ \frac{1}{12} & -\frac{2}{3} & 0 & \frac{2}{3} & -\frac{1}{12} \\ -\frac{1}{4} & \frac{5}{6} & \frac{3}{2} & -\frac{1}{2} & \frac{1}{12} \\ -\frac{25}{12} & 4 & -3 & \frac{4}{3} & \frac{1}{4} \end{pmatrix}$$

$$\gamma_0 = \frac{1}{70}, \quad \gamma_1 = \frac{8}{35}, \quad \gamma_2 = \frac{18}{35}, \quad \gamma_3 = \frac{8}{35}, \quad \gamma_4 = \frac{1}{70}$$

for  $r = 5$ .

If flux splitting is used and one more grid point is added, then we have

$$p'_j(x_i) = \sum_{l=0}^r d_{jl}^- f_{i+j+l-r+1}^-, \quad j = 0, \dots, r-1 \quad (2.15)$$

for  $f^-(u)$ , with

$$D^- = (d_{jl}^-)_{3 \times 4} = \begin{pmatrix} \frac{1}{6} & -1 & \frac{1}{2} & \frac{1}{3} \\ -\frac{1}{3} & -\frac{1}{2} & 1 & -\frac{1}{6} \\ -\frac{11}{6} & 3 & -\frac{3}{2} & \frac{1}{3} \end{pmatrix}$$

$$\gamma_0 = \frac{3}{10}, \quad \gamma_1 = \frac{3}{5}, \quad \gamma_2 = \frac{1}{10}$$

for  $r = 3$ , and

$$D^- = (d_{jl}^-)_{5 \times 6} = \begin{pmatrix} \frac{1}{20} & -\frac{1}{3} & 1 & -2 & \frac{13}{12} & \frac{1}{5} \\ -\frac{1}{30} & \frac{1}{4} & -1 & \frac{1}{3} & \frac{1}{2} & -\frac{1}{20} \\ \frac{1}{20} & -\frac{1}{2} & -\frac{1}{3} & 1 & -\frac{1}{4} & \frac{1}{30} \\ -\frac{1}{5} & -\frac{13}{12} & 2 & -1 & \frac{1}{3} & -\frac{1}{20} \\ -\frac{137}{60} & 5 & -5 & \frac{10}{3} & -\frac{5}{4} & \frac{1}{5} \end{pmatrix}$$

$$\gamma_0 = \frac{1}{126}, \quad \gamma_1 = \frac{10}{63}, \quad \gamma_2 = \frac{10}{21}, \quad \gamma_3 = \frac{20}{63}, \quad \gamma_4 = \frac{5}{126}$$

for  $r = 5$ . The approximation for  $f^+(u)$  is mirror symmetric with respect to  $x_i$ .

(d) Compute the smoothness indicators, denoted by  $\beta_j$ . We still use the same smoothness indicators as before:

$$\beta_j = \sum_{l=1}^{r-1} \int_{I_i} h^{2l-1} \left( \frac{d^l}{dx^l} p_j(x) \right)^2 dx. \quad (2.16)$$

We can write out these smoothness indicators  $\beta_j$  explicitly as quadratic forms of  $f_i$  in the stencil.

(e) As before, we compute the nonlinear weights based on the smoothness indicators

$$\omega_j = \frac{\bar{\omega}_j}{\sum_{l=0}^{r-1} \bar{\omega}_l}, \quad \bar{\omega}_j = \frac{\gamma_j}{(\varepsilon + \beta_j)^2}, \quad (2.17)$$

where  $\gamma_j$  are the linear weights determined in step (c) above, and  $\varepsilon$  is a small number to avoid the denominator becoming 0. As before, we use  $\varepsilon = 10^{-8}$  here in all the computations. The final WENO approximation is then given by

$$f(u)_x|_{x=x_i} \approx \sum_{j=0}^{r-1} \omega_j p'_j(x_i). \quad (2.18)$$

Following the above steps we can evolve the numerical solution from a time step to the next time step on a staggered mesh, and in the following time step we repeat the solution process and come back to the original mesh.

We remark that there are three WENO reconstruction or approximation steps at time level  $t^n$ , namely the WENO reconstruction from  $\{\bar{u}_i^n\}$  to  $\{u_{i+\frac{1}{2}}^n\}$ , the WENO reconstruction from  $\{\bar{u}_i^n\}$  to  $\{u_i^n\}$ , and the WENO approximation from  $\{u_i^n\}$  to  $\{f(u)_x|_{x=x_i}\}$ . However, the first two reconstructions share the same smoothness indicators, which is one of the most costly parts of the procedure. For each additional Runge–Kutta inner stage (there are three additional inner stages for the fourth-order Runge–Kutta method), only one WENO approximation from  $\{u_i\}$  to  $\{f(u)_x|_{x=x_i}\}$  is needed. This should be compared with a nonstaggered finite difference WENO scheme in [3, 7] where only one WENO reconstruction is needed per Runge–Kutta inner stage, including the first reconstruction at time level  $t^n$ .

For systems of conservation laws, such as the Euler equations of gas dynamics, all three WENO reconstructions and approximations (from  $\{\bar{u}_i^n\}$  to  $\{\bar{u}_{i+\frac{1}{2}}^n\}$ , from  $\{\bar{u}_i^n\}$  to  $\{u_i^n\}$ , and from  $\{u_i^n\}$  to  $\{f(u)_x|_{x=x_i}\}$ ) could either be performed in each component or in local characteristic directions. The local characteristic decomposition certainly increases the computational cost. It is usually noted in the literature that such local characteristic decomposition is unnecessary for central schemes. In fact this is also true for some noncentral schemes, e.g., [19]. However, most of such schemes are second-order, or at most third-order, accurate. In the following section of numerical experiments we will explore when and where it is necessary to perform such local characteristic decompositions when the order of accuracy is higher.

### 3. NUMERICAL RESULTS

In this section we present the results of our numerical experiments for the fifth- and ninth-order CWENO schemes with the fourth-order NCE Runge–Kutta method reviewed and developed in the previous section and compare them with the finite difference WENO schemes in [3, 7]. A uniform mesh with  $N$  cells is used for all the test cases, and the CFL number is taken as 0.4, except for the accuracy tests where a suitably reduced time step is used to guarantee that spatial error dominates.

#### 3.1. Accuracy Tests

We first test the accuracy of the schemes on linear scalar problems, nonlinear scalar problems, and nonlinear systems.

**TABLE I**  
 $u_t + u_x = 0; u(x, 0) = \sin(\pi x);$  CWENO-5 with Periodic Boundary  
 Conditions;  $t = 10; L_1$  and  $L_\infty$  Errors

$N$	$L_1$ error	$L_1$ order	$L_\infty$ error	$L_\infty$ order
10	4.31E-01		3.27E-01	
20	2.59E-02	4.06	1.80E-02	4.19
40	9.24E-04	4.81	7.21E-04	4.64
80	2.86E-05	5.01	2.50E-05	4.85
160	8.94E-07	5.00	7.97E-07	4.97
320	2.79E-08	5.00	2.54E-08	4.97
640	8.65E-10	5.01	7.52E-10	5.08
1280	2.63E-11	5.04	2.27E-11	5.05

EXAMPLE 3.1. We solve the following linear scalar problem

$$u_t + u_x = 0 \quad (3.1)$$

with two different initial conditions,  $u(x, 0) = \sin(\pi x)$  and  $u(x, 0) = \sin^4(\pi x)$ , with 2-periodic boundary conditions. The second initial condition is typically more difficult to ENO type schemes to achieve a full order of accuracy [26]. We compute the solution up to  $t = 10$ , i.e., after five time periods. The results are shown in Tables I–IV. We can see that both the fifth-order central WENO (CWENO-5) and the ninth-order central WENO (CWENO-9) schemes achieve their designed order of accuracy for both initial conditions.

EXAMPLE 3.2. We solve the following nonlinear scalar Burgers equation

$$u_t + \left(\frac{u^2}{2}\right)_x = 0 \quad (3.2)$$

with the initial condition  $u(x, 0) = 0.5 + \sin(\pi x)$ , with 2-periodic boundary conditions. When  $t = 0.5/\pi$  the solution is still smooth, and the errors and numerical orders of accuracy are shown in Tables V and VI. We can see that both the fifth-order central WENO (CWENO-5) and the ninth-order central WENO (CWENO-9) schemes achieve their designed order of accuracy.

**TABLE II**  
 $u_t + u_x = 0; u(x, 0) = \sin^4(\pi x);$  CWENO-5 with Periodic Boundary  
 Conditions;  $t = 10; L_1$  and  $L_\infty$  Errors

$N$	$L_1$ error	$L_1$ order	$L_\infty$ error	$L_\infty$ order
10	6.77E-01		4.54E-01	
20	2.10E-01	1.69	2.43E-01	0.90
40	3.81E-02	2.46	4.00E-02	2.60
80	4.04E-03	3.24	8.56E-03	2.22
160	2.71E-04	3.90	1.33E-03	2.69
320	6.90E-06	5.30	4.20E-05	4.98
640	1.40E-07	5.62	7.72E-07	5.77
1280	3.46E-09	5.34	1.32E-08	5.87

**TABLE III**  
 $u_t + u_x = 0; u(x, 0) = \sin(\pi x);$  CWENO-9 with Periodic Boundary  
 Conditions;  $t = 10; L_1$  and  $L_\infty$  Errors

$N$	$L_1$ error	$L_1$ order	$L_\infty$ error	$L_\infty$ order
10	1.48E-02	—	1.09E-02	—
20	6.68E-05	7.79	6.26E-05	7.44
40	1.15E-07	9.18	1.26E-07	8.95
80	2.20E-10	9.03	2.63E-10	8.91

**TABLE IV**  
 $u_t + u_x = 0; u(x, 0) = \sin^4(\pi x);$  CWENO-9 with Periodic Boundary  
 Conditions;  $t = 10; L_1$  and  $L_\infty$  Errors

$N$	$L_1$ error	$L_1$ order	$L_\infty$ error	$L_\infty$ order
10	6.52E-01	—	4.08E-01	—
20	1.51E-01	2.11	1.52E-01	1.42
40	6.86E-03	4.46	1.05E-02	3.86
80	1.37E-05	8.97	2.86E-05	8.51
160	5.72E-08	7.90	1.26E-07	7.82
320	1.07E-10	9.06	2.83E-10	8.80

**TABLE V**  
 $u_t + (\frac{u^2}{2})_x = 0; u(x, 0) = 0.5 + \sin(\pi x);$  CWENO-5 with Periodic  
 Boundary Conditions;  $t = 0.5/\pi; L_1$  and  $L_\infty$  Errors

$N$	$L_1$ error	$L_1$ order	$L_\infty$ error	$L_\infty$ order
10	2.18E-02	—	4.02E-02	—
20	4.10E-03	2.41	1.10E-02	1.87
40	1.31E-04	4.97	6.70E-04	4.04
80	3.86E-06	5.08	2.56E-05	4.71
160	1.12E-07	5.11	7.76E-07	5.04
320	3.19E-09	5.14	2.21E-08	5.13
640	9.45E-11	5.08	6.48E-10	5.09
1280	2.77E-12	5.09	1.82E-11	5.15

**TABLE VI**  
 $u_t + (\frac{u^2}{2})_x = 0; u(x, 0) = 0.5 + \sin(\pi x);$  CWENO-9 with Periodic  
 Boundary Conditions;  $t = 0.5/\pi; L_1$  and  $L_\infty$  Errors

$N$	$L_1$ error	$L_1$ order	$L_\infty$ error	$L_\infty$ order
10	5.29E-02	—	9.81E-02	—
20	4.00E-03	3.72	1.22E-02	3.01
40	1.06E-04	5.24	4.68E-04	4.70
80	7.02E-07	7.23	5.78E-06	6.34
160	1.91E-09	8.52	1.87E-08	8.28
320	3.32E-12	9.17	3.39E-11	9.11

TABLE VII

**Euler Equations;  $\rho(x, 0) = 1 + 0.2 \sin(\pi x)$ ,  $v(x, 0) = 1$ ,  $p(x, 0) = 1$ ;  
CWENO-5 with Periodic Boundary Conditions;  $t = 2$ ;  $L_1$  and  $L_\infty$  Errors  
of Density  $\rho$**

$N$	$L_1$ error	$L_1$ order	$L_\infty$ error	$L_\infty$ order
20	1.79E-03		1.49E-03	
40	1.03E-04	4.11	1.13E-04	3.72
80	6.46E-06	4.00	1.05E-05	3.43
160	1.00E-07	6.01	1.63E-07	6.01
320	1.19E-09	6.40	1.29E-09	6.97
640	3.82E-11	4.96	3.64E-11	5.15
1280	1.18E-12	5.01	1.07E-12	5.09

EXAMPLE 3.3. We solve the following nonlinear system of Euler equations

$$u_t + f(u)_x = 0 \quad (3.3)$$

with

$$u = (\rho, \rho v, E)^T, \quad f(u) = (\rho v, \rho v^2 + p, v(E + p))^T.$$

Here  $\rho$  is the density,  $v$  is the velocity,  $E$  is the total energy,  $p$  is the pressure, related to the total energy by  $E = \frac{p}{\gamma-1} + \frac{1}{2}\rho v^2$  with  $\gamma = 1.4$ . The initial condition is set to be  $\rho(x, 0) = 1 + 0.2 \sin(\pi x)$ ,  $v(x, 0) = 1$ ,  $p(x, 0) = 1$ , with 2-periodic boundary conditions. The exact solution is  $\rho(x, t) = 1 + 0.2 \sin(\pi(x - t))$ ,  $v = 1$ ,  $p = 1$ . We compute the solution up to  $t = 2$  using componentwise WENO reconstructions and various characteristic and flux-splitting WENO reconstructions outlined at the end of the last section; i.e., we perform one, two, or three out of the three WENO reconstructions and approximations (from  $\{\bar{u}_i^n\}$  to  $\{\bar{u}_{i+\frac{1}{2}}^n\}$ , from  $\{\bar{u}_i^n\}$  to  $\{u_i^n\}$ , and from  $\{u_i^n\}$  to  $\{f(u)_x|_{x=x_i}\}$ ) in local characteristic directions and the remaining componentwise reconstructions. For this smooth test case, all cases produce similar errors and orders of accuracy. The errors and numerical orders of accuracy of the density  $\rho$  for the componentwise WENO reconstructions are shown in Tables VII and VIII. We can see that both the fifth-order central WENO (CWENO-5) and the ninth-order central WENO (CWENO-9) schemes achieve their designed order of accuracy.

TABLE VIII

**Euler Equations;  $\rho(x, 0) = 1 + 0.2 \sin(\pi x)$ ,  $v(x, 0) = 1$ ,  $p(x, 0) = 1$ ;  
CWENO-9 with Periodic Boundary Conditions;  $t = 2$ ;  $L_1$  and  $L_\infty$  Errors  
of Density  $\rho$**

$N$	$L_1$ error	$L_1$ order	$L_\infty$ error	$L_\infty$ order
10	2.92E-04	—	2.26E-04	—
20	6.40E-07	8.83	5.07E-07	8.80
40	1.29E-09	8.96	1.01E-09	8.97
80	2.53E-12	8.99	1.99E-12	8.99

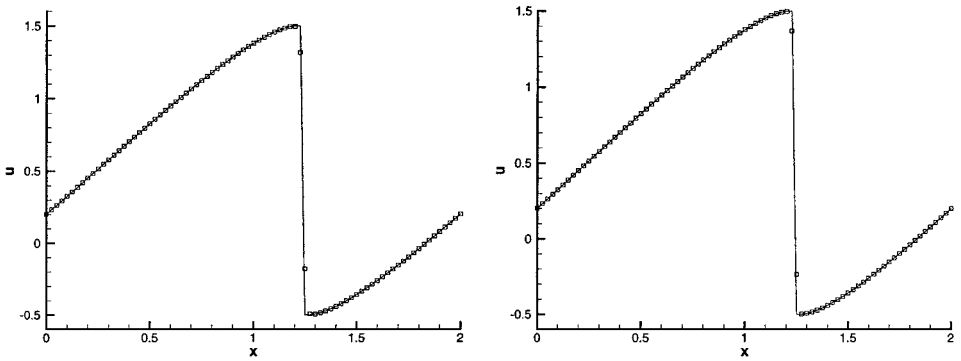


**FIG. 1.** Burgers equation.  $u(x, 0) = 0.5 + \sin(\pi x)$ .  $t = 1.5/\pi$ .  $N = 80$  points. Left: CWENO-5; right: CWENO-9. Solid line: exact solution; squares: computed solution.

### 3.2. Test Cases with Shocks

**EXAMPLE 3.4.** We solve the same nonlinear Burgers equation (3.2) as that in Example 3.2 with the same initial condition  $u(x, 0) = 0.5 + \sin(\pi x)$ , except that we now plot the results at  $t = 1.5/\pi$  when a shock has already appeared in the solution. In Fig. 1, the solutions of CWENO-5 (left) and CWENO-9 (right) with  $N = 80$  grid points are shown. The solid line is the exact solution. We can see that both schemes give nonoscillatory shock transitions for this problem.

**EXAMPLE 3.5.** We solve the nonlinear nonconvex scalar Buckley–Leverett problem

$$u_t + \left( \frac{4u^2}{4u^2 + (1-u)^2} \right)_x = 0 \quad (3.4)$$

with the initial data  $u = 1$  when  $-\frac{1}{2} \leq x \leq 0$  and  $u = 0$  elsewhere. The solution is computed up to  $t = 0.4$ . The exact solution is a shock-rarefaction-contact discontinuity mixture. We remark that some high-order schemes may fail to converge to the correct entropy solution for this problem. In Fig. 2, the solutions of CWENO-5 (left) and CWENO-9 (right) with  $N = 81$  grid points are shown. The solid line is the exact solution. We can see that both schemes give good resolutions to the correct entropy solution for this problem.

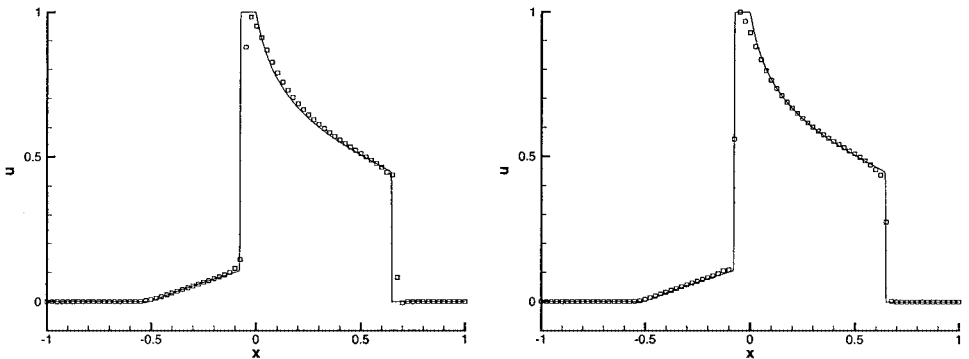


**FIG. 2.** The Buckley–Leverett problem.  $t = 0.4$ .  $N = 81$  points. Left: CWENO-5; right: CWENO-9. Solid line: exact solution; squares: computed solution.

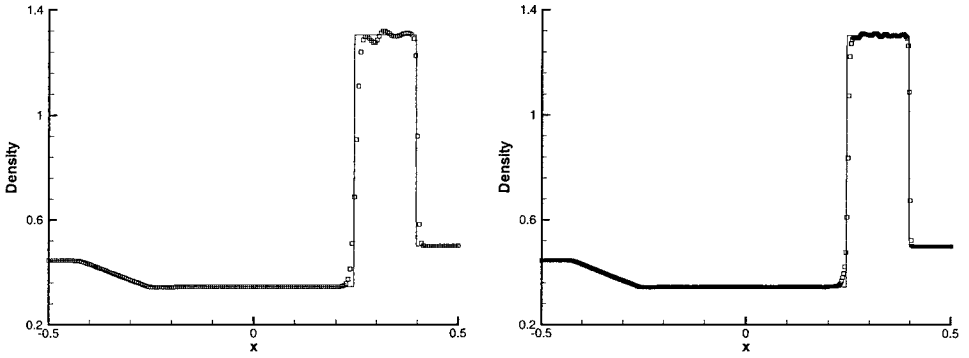


**FIG. 3.** The Lax problem.  $t = 0.16$ . CWENO-5 scheme with componentwise WENO reconstructions. Left:  $N = 200$  grid points; right:  $N = 400$  grid points. Solid line: exact solution; squares: computed solution.

**EXAMPLE 3.6.** We solve the Euler equations (3.3) with a Riemann initial condition for the Lax problem:

$$(\rho, v, p) = (0.445, 0.698, 3.528) \quad \text{for } x \leq 0; \quad (\rho, v, p) = (0.5, 0, 0.571) \quad \text{for } x > 0.$$

The computed density  $\rho$  is plotted at  $t = 0.16$  against the exact solution. In Fig. 3 we plot the solution with CWENO-5 using componentwise WENO reconstruction, with  $N = 200$  grid points (left) and  $N = 400$  grid points (right). We can see that the results are oscillatory but the oscillations become less significant when the mesh is refined. For a comparison, in Fig. 4 we plot the solution with the finite difference fifth-order WENO scheme on a nonstaggered mesh in [7] using componentwise reconstructions, also with  $N = 200$  grid points (left) and  $N = 400$  grid points (right). We can see that these are also oscillatory and the oscillations are a bit more serious than that for the central CWENO-5 scheme.

We repeat the experiment for the CWENO-9 schemes using componentwise WENO reconstructions in Fig. 5, and for the ninth-order finite difference WENO scheme on a nonstaggered mesh in [3] in Fig. 6. We can see that the oscillations increase when the order of accuracy is increased. Also, as before, the nonstaggered WENO scheme has more oscillations than the central CWENO-9 scheme.

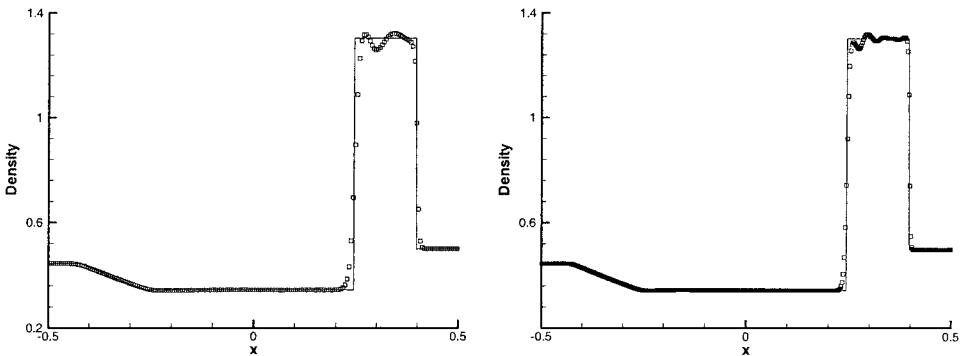


**FIG. 4.** The Lax problem.  $t = 0.16$ . WENO-5 finite difference scheme [7] with componentwise reconstruction. Left:  $N = 200$  grid points; right:  $N = 400$  grid points. Solid line: exact solution; squares: computed solution.

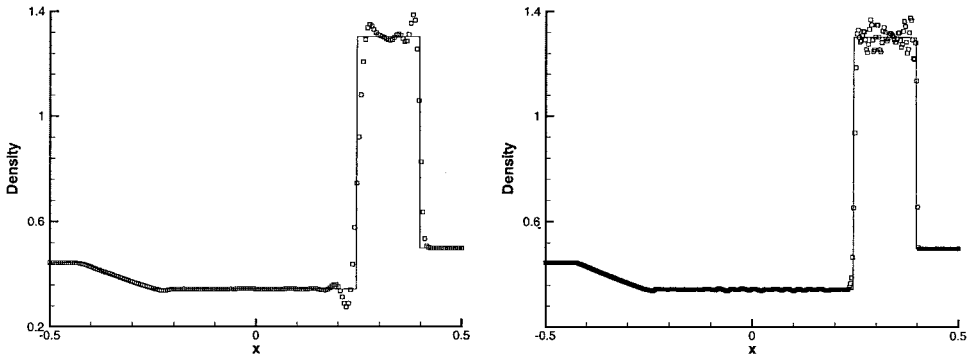


**FIG. 5.** The Lax problem.  $t = 0.16$ . CWENO-9 scheme with componentwise WENO reconstructions. Left:  $N = 200$  grid points; right:  $N = 400$  grid points. Solid line: exact solution; squares: computed solution.

We have also experimented with using a single quantity (e.g., density  $\rho$ ) for computing the smoothness indicator for all components. The results are similarly oscillatory.

We conclude from this example that the componentwise WENO scheme will become more oscillatory when the order of accuracy increases, both for the central WENO schemes and for the usual finite difference WENO schemes on a nonstaggered mesh, although the central WENO with a staggered mesh tends to give smaller oscillations.

We demonstrate that a local characteristic decomposition in the WENO reconstruction procedure significantly reduces the oscillations. In fact, we found after extensive numerical experiments that, as long as one does the local characteristic decomposition for the reconstruction from  $\{\bar{u}_i^n\}$  to  $\{\bar{u}_{i+\frac{1}{2}}^n\}$ , one can still use componentwise WENO reconstruction from  $\{\bar{u}_i^n\}$  to  $\{u_i^n\}$  and componentwise WENO approximation from  $\{u_i^n\}$  to  $\{f(u)_x|_{x=x_i}\}$  and significantly reduce the spurious oscillations. See Fig. 7 for the results of the CWENO-5 scheme and Fig. 8 for the results of the CWENO-9 scheme. For comparison, we plot the results of the fifth-order finite difference WENO scheme using local characteristic decompositions on a nonstaggered mesh [7] in Fig. 9. and the ninth-order finite difference WENO scheme using local characteristic decompositions on a nonstaggered mesh [3] in Fig. 10. We can see that when local characteristic decomposition is used, both the central

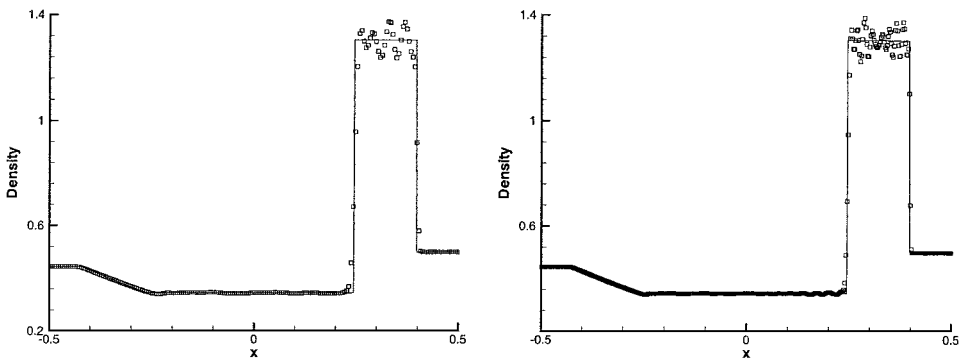


**FIG. 6.** The Lax problem.  $t = 0.16$ . WENO-9 finite difference scheme [3] with componentwise reconstruction. Left:  $N = 200$  grid points; right:  $N = 400$  grid points. Solid line: exact solution; squares: computed solution.

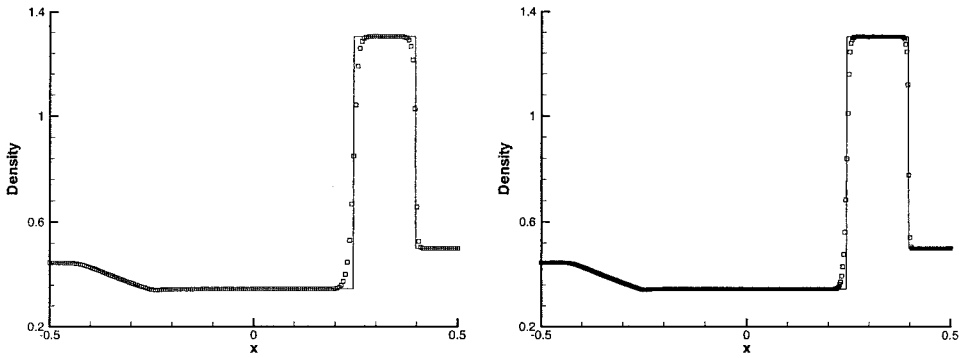


**FIG. 7.** The Lax problem.  $t = 0.16$ . CWENO-5 scheme with local characteristic decomposition for the WENO reconstruction of  $\bar{u}_{j+\frac{1}{2}}$ . Left:  $N = 200$  grid points; right:  $N = 400$  grid points. Solid line: exact solution; squares: computed solution.

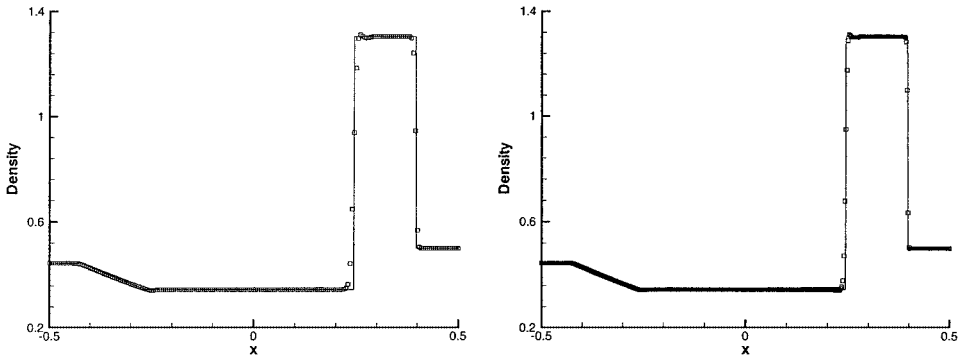


**FIG. 8.** The Lax problem.  $t = 0.16$ . CWENO-9 scheme with local characteristic decomposition for the WENO reconstruction of  $\bar{u}_{j+\frac{1}{2}}$ . Left:  $N = 200$  grid points; right:  $N = 400$  grid points. Solid line: exact solution; squares: computed solution.

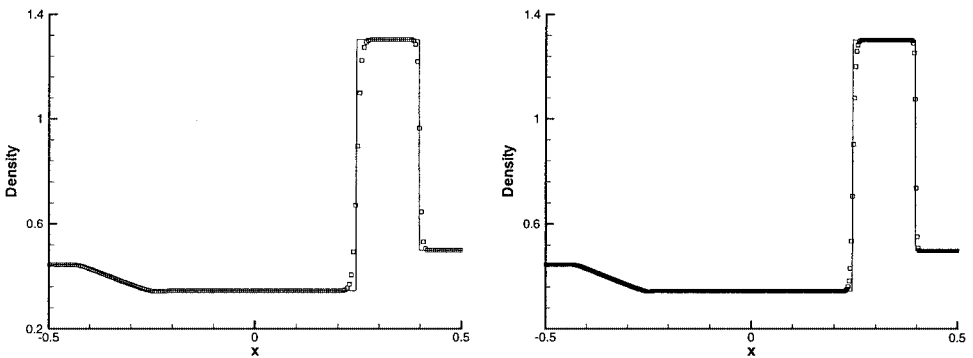


**FIG. 9.** The Lax problem.  $t = 0.16$ . WENO-5 finite difference scheme [7] with local characteristic decomposition. Left:  $N = 200$  grid points; right:  $N = 400$  grid points. Solid line: exact solution; squares: computed solution.

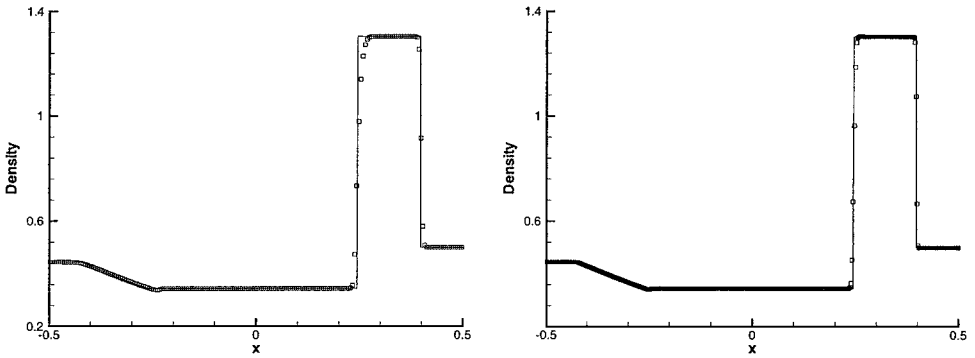


**FIG. 10.** The Lax problem.  $t = 0.16$ . WENO-9 finite difference scheme [3] with local characteristic decomposition. Left:  $N = 200$  grid points; right:  $N = 400$  grid points. Solid line: exact solution; squares: computed solution.

WENO schemes based on staggered mesh and the finite difference WENO schemes based on nonstaggered mesh give beautiful essentially nonoscillatory results.

**EXAMPLE 3.7.** The previous examples contain only shocks and simple smooth region solutions (almost piecewise linear), for which shock resolution is the main concern and usually a good second-order nonoscillatory scheme would give satisfactory results. There is little advantage in using higher order schemes for such cases. We have been using them in the numerical experiments mainly to demonstrate the nonoscillatory properties of the high-order schemes. A higher order scheme would show its advantage when the solution contains both shocks and complex smooth region structures. A typical example for this is the problem of shock interaction with entropy waves [29]. We solve the Euler equations (3.3) with a moving Mach = 3 shock interacting with sine waves in density; i.e., initially

$$(\rho, v, p) = (3.857143, 2.629369, 10.333333) \quad \text{for } x < -4;$$

$$(\rho, v, p) = (1 + \varepsilon \sin 5x, 0, 1) \quad \text{for } x \geq -4.$$

Here we take  $\varepsilon = 0.2$ . The computed density  $\rho$  is plotted at  $t = 1.8$  against the reference

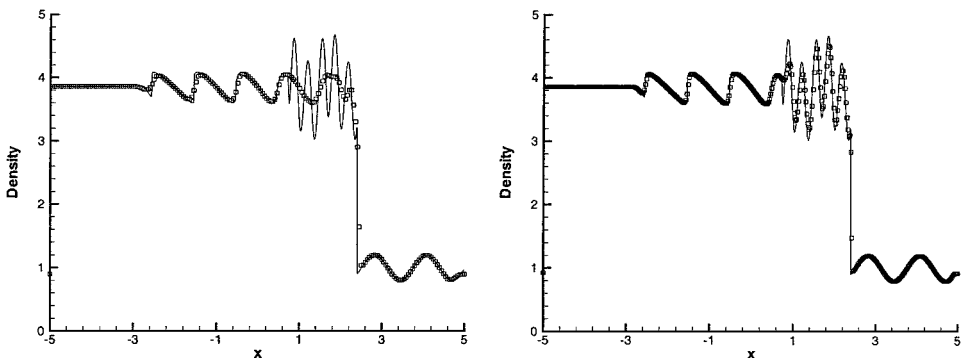


**FIG. 11.** The shock density wave interaction problem.  $t = 1.8$ . CWENO-5 scheme with local characteristic decomposition for the WENO reconstruction of  $\bar{u}_{j+\frac{1}{2}}$ . Left:  $N = 200$  grid points; right:  $N = 400$  grid points. Solid line: "exact solution"; squares: computed solution.

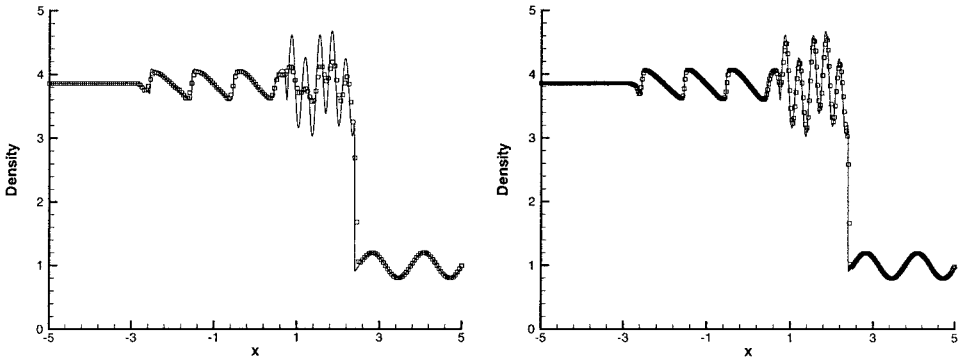


**FIG. 12.** The shock density wave interaction problem.  $t = 1.8$  CWENO-9 scheme with local characteristic decomposition for the WENO reconstruction of  $\bar{u}_{j+\frac{1}{2}}$ . Left:  $N = 200$  grid points; right:  $N = 400$  grid points. Solid line: “exact solution”; squares: computed solution.

solution, which is a converged solution computed by the fifth-order finite difference WENO scheme [7] with 2000 grid points.

In Figs.11 and 12 we show the results of the CWENO-5 scheme and the CWENO-9 scheme, respectively, using the local characteristic decomposition for the reconstruction from  $\{\bar{u}_i^n\}$  to  $\{\bar{u}_{i+\frac{1}{2}}^n\}$  and componentwise WENO reconstruction from  $\{\bar{u}_i^n\}$  to  $\{u_i^n\}$  and componentwise WENO approximation from  $\{u_i^n\}$  to  $\{f(u)_x|_{x=x_i}\}$ . For comparison, we plot the results of the fifth-order finite difference WENO scheme using local characteristic decompositions on a nonstaggered mesh [7] in Fig. 13 and the ninth-order finite difference WENO scheme using local characteristic decompositions on a nonstaggered mesh [3] in Fig. 14. We can see that higher order schemes give better resolutions to the complex wave patterns after the shock entropy wave interaction, for the same number of grid points. For this problem, the componentwise CWENO and WENO schemes also work very well. We do not show the results to save space.

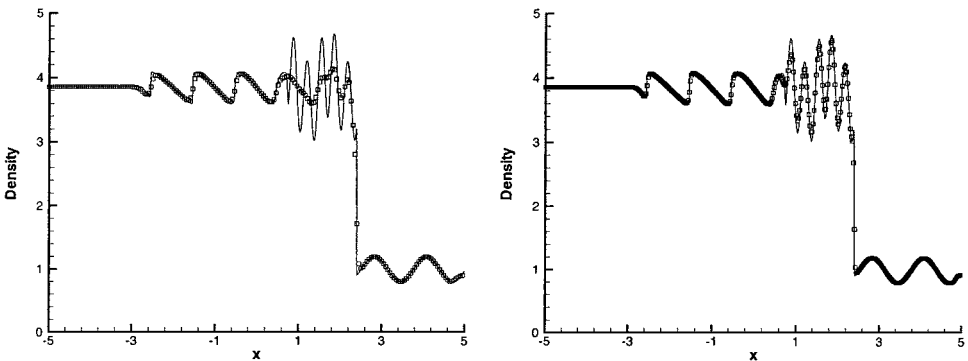


**FIG. 13.** The shock density wave interaction problem.  $t = 1.8$ , WENO-5 finite difference scheme [7] with local characteristic decomposition. Left:  $N = 200$  grid points; right:  $N = 400$  grid points. Solid line: “exact solution”; squares: computed solution.

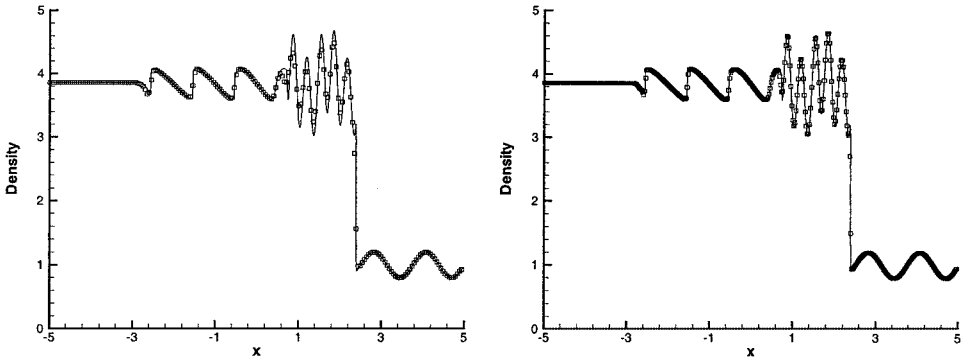


**FIG. 14.** The shock density wave interaction problem.  $t = 1.8$ . WENO-9 finite difference scheme [3] with local characteristic decomposition. Left:  $N = 200$  grid points; right:  $N = 400$  grid points. Solid line: “exact solution”; squares: computed solution.

#### 4. CONCLUDING REMARKS

In this paper we reviewed and developed fifth- and ninth-order central WENO schemes based on staggered meshes. Negative linear weights appeared and they were treated using the recently developed splitting technique of Shi *et al.* [25]. Numerical examples were given to verify the order of accuracy of these schemes. Simulations with discontinuous solutions for the Euler equations demonstrated that componentwise WENO reconstruction would yield oscillatory results and the oscillations increased with increased order of accuracy, both for the central WENO schemes based on staggered meshes and for the finite difference WENO schemes based on nonstaggered meshes [3, 7]. If a local characteristic decomposition was used in the reconstruction, both for the central WENO schemes based on staggered meshes and for the finite difference WENO schemes based on nonstaggered meshes, essentially nonoscillatory solutions could be obtained. The local characteristic decomposition increased the computational cost significantly, so it is problem dependent whether one should use it or simply tolerate the spurious oscillations, if they do not lead to nonlinear instability such as negative density or pressure for the Euler equations. These high-order schemes are useful to simulate problems where shocks and complex smooth region structures coexist, such as the problem of shock interaction with entropy waves.

#### REFERENCES

1. P. Arminjon and M.-C. Viallon, Généralisation du schéma de Nessyahu-Tadmor pour une Équation hyperbolique à deux dimensions d’espace, *C. R. Acad. Sci. Paris* **320**, 85 (1995).
2. P. Arminjon, M.-C. Viallon, and A. Madrane, A finite volume extension of the Lax–Friedrichs and Nessyahu–Tadmor schemes for conservation laws on unstructured grids, *Int. J. Comp. Fluid Dynam.* **9**, 1 (1997).
3. D. S. Balsara and C.-W. Shu, Monotonicity preserving weighted essentially non-oscillatory schemes with increasingly high order of accuracy, *J. Comput. Phys.* **160**, 405 (2000).
4. F. Bianco, G. Puppo, and G. Russo, High-order central schemes for hyperbolic systems of conservation laws, *SIAM J. Sci. Comput.* **21**, 294 (1999).
5. A. Harten, B. Engquist, S. Osher, and S. Chakravathy, Uniformly high order accurate essentially non-oscillatory schemes, III, *J. Comput. Phys.* **71**, 231 (1987).

6. C. Hu and C.-W. Shu, Weighted essentially non-oscillatory schemes on triangular meshes, *J. Comput. Phys.* **150**, 97 (1999).
7. G.-S. Jiang and C.-W. Shu, Efficient implementation of weighted ENO schemes, *J. Comput. Phys.* **126**, 202 (1996).
8. G.-S. Jiang and E. Tadmor, Non-oscillatory central schemes for multidimensional hyperbolic conservation laws, *SIAM J. Sci. Comput.* **19**, 1892 (1998).
9. G.-S. Jiang, D. Levy, C.-T. Lin, S. Osher, and E. Tadmor, High-resolution non-oscillatory central schemes with non-staggered grids for hyperbolic conservation laws, *SIAM J. Numer. Anal.* **35**, 2147 (1998).
10. A. Kurganov and D. Levy, A third-order semidiscrete central scheme for conservation laws and convection–diffusion equations, *SIAM J. Sci. Comput.* **22**, 1461 (2000).
11. A. Kurganov, S. Noelle, and G. Petrova, Semi-discrete central-upwind schemes for hyperbolic conservation laws and Hamilton–Jacobi equations, *SIAM J. Sci. Comput.* **23**, 707 (2001).
12. A. Kurganov and G. Petrova, Central schemes and contact discontinuities, *Math. Model. Numer. Anal.* **34**, 1259 (2000).
13. A. Kurganov and G. Petrova, A third order semi-discrete genuinely multidimensional central scheme for hyperbolic conservation laws and related problems, *Numer. Math.* **88**, 683 (2001).
14. A. Kurganov and E. Tadmor, New high-resolution central schemes for nonlinear conservation laws and convection–diffusion equations, *J. Comput. Phys.* **160**, 214 (2000).
15. D. Levy, G. Puppo, and G. Russo, Central WENO schemes for hyperbolic systems of conservation laws, *Math. Model. Numer. Anal.* **33**, 547 (1999).
16. D. Levy, G. Puppo, and G. Russo, Compact central WENO schemes for multidimensional conservation laws, *SIAM J. Sci. Comput.* **22**, 656 (2000).
17. D. Levy, G. Puppo, and G. Russo, On the behavior of the total variation in CWENO methods for conservation laws, *Appl. Numer. Math.* **33**, 407 (2000).
18. D. Levy, G. Puppo, and G. Russo, A third order central WENO scheme for 2D conservation laws, *Appl. Numer. Math.* **33**, 415 (2000).
19. X. D. Liu and S. Osher, Convex ENO high order multi-dimensional schemes without field by field decomposition or staggered grids, *J. Comput. Phys.* **142**, 304 (1998).
20. X. D. Liu and S. Osher, Nonoscillatory high order accurate self-similar maximum principle satisfying shock capturing schemes I, *SIAM. J. Numer. Anal.* **33**, 760 (1996).
21. X. D. Liu and E. Tadmor, Third order nonoscillatory central scheme for hyperbolic conservation laws, *Numer. Math.* **79**, 397 (1998).
22. X. D. Liu, S. Osher, and T. Chan, Weighted essentially non-oscillatory schemes, *J. Comput. Phys.* **115**, 200 (1994).
23. H. Nessyahu and E. Tadmor, Non-oscillatory central differencing for hyperbolic conservation laws, *J. Comput. Phys.* **87**, 408 (1990).
24. R. Sanders and A. Weiser, High resolution staggered mesh approach for nonlinear hyperbolic systems of conservation laws, *J. Comput. Phys.* **101**, 314 (1992).
25. J. Shi, C. Hu, and C.-W. Shu, A technique of treating negative weights in WENO schemes, *J. Comput. Phys.* **175**, 108 (2002).
26. C.-W. Shu, Numerical experiments on the accuracy of ENO and modified ENO schemes, *J. Sci. Comput.* **5**, 127 (1990).
27. C.-W. Shu, Essentially non-oscillatory and weighted essentially non-oscillatory schemes for hyperbolic conservation laws, in *Advanced Numerical Approximation of Nonlinear Hyperbolic Equations*, edited by B. Cockburn, C. Johnson, C.-W. Shu, and E. Tadmor, Lect. Notes in Math. (Springer-Verlag, Berlin/New York, 1998), Vol. 1697, p. 325.
28. C.-W. Shu and S. Osher, Efficient implementation of essentially non-oscillatory shock capturing schemes, *J. Comput. Phys.* **77**, 439 (1988).
29. C.-W. Shu and S. Osher, Efficient implementation of essentially non-oscillatory shock capturing schemes, II, *J. Comput. Phys.* **83**, 32 (1989).
30. M. Zennaro, Natural continuous extensions of Runge–Kutta methods, *Math. Comput.* **46**, 119 (1986).